# Three-dimensional interpretation of magnetic and gravity anomalies using the finite-difference similarity transform

GEOPHYSICS, VOL. 75, NO. 4 (JULY-AUGUST 2010); P. L79–L90, 8 FIGS., 4 TABLES.
10.1190/1.3453765



# Three-dimensional interpretation of magnetic and gravity anomalies using the finite-difference similarity transform

Daniela Gerovska[1], Marcos J. Araúzo-Bravo[2], Kathryn Whaler[1], Petar Stavrev[3], and Alan Reid[4]

## ABSTRACT

We present an automatic procedure for interpretation of magnetic or gravity gridded anomalies based on the finite-difference similarity transform (FDST). It is called MaGSoundFDST (magnetic and gravity sounding based on the finite-difference similarity transform) and uses a "focusing" principle in contrast to deriving multiple clusters of many solutions as in the widely used Euler deconvolution method. The source parameters are characterized by isolated solutions, and the interpreter obtains parallel images showing the horizontal position, depth, and structural index $N$ value. The underlying principle is that the FDST of a potential field anomaly becomes zero or linear at all observation points when the central point of similarity (CPS) of the transform coincides with a source field's singular point and a correct $N$ value is used. The procedure involves calculating a 3D function that evaluates the linearity of the FDST for a series of $N$ values, using a moving window and sounding the subsurface along a vertical line under each window center. We then combine the 3D results for different $N$ values into a single map whose minima determine the horizontal position of the sources. The $N$ value and the CPS depth associated with each minimum determine the $N$ value and depth of the corresponding source. Only one estimate characterizes a simple source, which is a major advantage over other window-based procedures. MaGSoundFDST uses only the measured anomalous field and its upward continuation, thus avoiding the direct use of field derivatives. It is independent of the magnetization-vector direction in the magnetic data case. The procedure accounts for a linear background of local gravity or magnetic anomalies and has been applied effectively to several cases of synthetic and real data. MaGSoundFDST shares common features with the magnetic and gravity sounding based on the differential similarity transform (MaGSoundDST) but is more stable in estimating depth and structural index in the presence of random noise.

## INTRODUCTION

The depth and shape of simple magnetic or gravity sources can be estimated using Euler's differential equation for homogeneous functions in 2D (Thompson, 1982) and 3D (Reid et al., 1990) inverse problems. This approach, known as Euler deconvolution, involves the data and their first-order derivatives in a system of linear equations in relation to the source coordinates. Each anomaly $A(x,y,z)$ is treated as the field of one singular point at $M(x_0,y_0,z_0)$. Thus, Euler's differential equation takes the form

$$(x-x_0)\frac{\partial A}{\partial x}+(y-y_0)\frac{\partial A}{\partial y}+(z-z_0)\frac{\partial A}{\partial z}=nA, \qquad (1)$$

where $\partial A/\partial x$, $\partial A/\partial y$, and $\partial A/\partial z$ are the components of the anomaly's gradient and $n$ is the degree of homogeneity of $A$. The degree of homogeneity, a parameter indicative of the source geometry, is prescribed (Thompson, 1982; Reid et al., 1990) or estimated (Stavrev, 1997; Hsu, 2002; Gerovska and Araúzo-Bravo, 2003; FitzGerald et al., 2004; Keating and Pilkington, 2004; Gerovska et al., 2005).

Manuscript received by the Editor 3 August 2009; revised manuscript received 1 March 2010; published online 29 September 2010.
[1]University of Edinburgh, School of GeoSciences, Edinburgh, U.K. E-mail: dgerovsk@staffmail.ed.ac.uk; kathy.whaler@ed.ac.uk.
[2]Max Planck Institute for Molecular Biomedicine, Münster, Germany. E-mail: marcos.arauzo@mpi-mail.mpg.de.
[3]University of Mining and Geology St. Ivan Rilski, Department of Applied Geophysics, Sofia, Bulgaria. E-mail: pstavrev@mail.bg.
[4]Reid Geophysics, Eastbourne, U.K. E-mail: alan@reid-geophys.co.uk.

As an alternative to inversion for source parameters using equation 1, the definition equation for a homogeneous function (Courant and John, 1965)

$$f(tv_1,tv_2,\ldots,tv_i,\ldots,tv_j) = t^n f(v_1,v_2,\ldots,v_i,\ldots,v_j), \quad (2)$$

where $\mathbf{v} = (v_1,v_2,\ldots,v_i,\ldots,v_j)$ is the full set of variables to which the function $f$ shows the homogeneity and $t$ is a coefficient, can be used directly for the same purpose. The wavelet transform (Boukerbout and Gibert, 2006; Fedi, 2007; Sailhac et al., 2009) and the similarity transform (Stavrev, 1997; Stavrev et al., 2006, 2009; Gerovska et al., 2010) are examples of the successful application of this approach.

Boukerbout and Gibert (2006) propose an inversion for locating the sources along profiles detected by the Radon transform of gridded data, based on calculating a series of complex analyzing Poisson wavelets (ridgelet transforms) — upward-continued analytic signals — for different dilation values. In turn, the dilation values correspond to different continuation heights. The apex of the conical pattern of the phase of the complex ridgelet transform determines the location of the source. Fedi et al. (2009) propose a similar method; however, they form a redundant set of ridges of first-order derivatives of the field. The continuous wavelet transform (CWT) estimates size and direction of extended sources (for a review of CWT inversion methods, see Sailhac et al., 2009). Fedi (2007) introduces a scaling function as the derivative of the logarithm of the potential field with respect to the logarithm of the depth to form a transformation, the extreme points of which determine the source locations.

Stavrev (1997) and Stavrev et al. (2006, 2009) explain the physical and geometric sense of equation 2 with respect to potential fields. Stavrev et al. (2006, 2009) use the finite-difference similarity transform (FDST) and the differential similarity transform (DST) to propose profile inversion algorithms for the location and structural index of 2D sources. They build upon the property that the FDST and DST functions become linear or zero for correct values of the location and the source's degree of homogeneity $n$. Gerovska et al. (2010) present an automatic procedure, MaGSoundDST, to invert grid-anomaly data for location and structural index of sources, based on the DST.

Here, we present an automatic 3D inversion procedure called magnetic and gravity sounding based on the finite-difference similarity transform (MaGSoundFDST) for interpreting magnetic and gravity data grids. Finite-difference similarity transforms are generated from a set of central points of similarity (CPS), distributed along a regular 3D grid under the measurement surface, for a set of degrees of homogeneity $n$. As in other methods (e.g., Fedi and Rapolla, 1999), the ambiguity of the determined source parameters is decreased by using a priori information, the assumed depth of the CPS grid. The FDSTs are sensitive to the distance between a CPS and the source. The CPS and the $n$ value that give a minimum value of the respective FDST indicate the source's position and shape. The technique accounts for a linear background in the data.

The MaGSoundDST (Gerovska et al., 2010) algorithm includes an automatic technique to obtain a single solution for each assumed source. We apply the same technique to an objective function derived from the FDST, which allows for better noise rejection while obtaining one estimate per simple source by projecting a set of 3D functions onto a 2D horizontal surface. Thus, we avoid numerous spurious solutions per single simple source that are characteristic of conventional Euler deconvolution techniques and other window-based methods.

## METHOD

### Theory

The potential fields used in applied geophysics can be described in terms of affine geometry. In a 3D affine space, the transform of similarity is a linear transform of Cartesian coordinates under the equations

$$x' = tx + (1-t)a, \quad y' = ty + (1-t)b,$$

$$z' = tz + (1-t)c, \quad (3)$$

where $(x,y,z)$ for a 3D potential field indicates the coordinates of the observation points and the source points. In equation 3, $(x',y',z')$ are the coordinates of their respective similar images, $(a,b,c)$ are the coordinates of a CPS $C$, and $t$ is a coefficient of similarity. The similarity transform can be applied to magnetic or gravity anomalies $A(x,y,z)$. For a coefficient of similarity $t > 1$ and a parameter $n$,

$$A'(x',y',z') = t^n A(x,y,z) \quad (4)$$

gives the direct similarity transform $A'$ of $A$.

The normalized FDST for an anomaly $A$ (Stavrev, 1997) is defined as the difference $D$ between the similarly transformed field $A'$ at point $P'$ and the original field $A$ in the same point $P'(x',y',z')$, normalized by $t-1$, i.e.,

$$D(x',y',z') = \frac{A'(x',y',z') - A(x',y',z')}{t-1}. \quad (5)$$

In equation 5, $A(x',y',z')$ is the upward continuation of the original field $A(x,y,z)$ or a measured field (e.g., from airborne surveys) at point $P'(x',y',z')$.

The FDSTs are sensitive to the distance between the CPS and the source. Their amplitudes decrease as the distance between the CPS and the source decreases (Stavrev et al., 2006). Some of the frequently used interpretation models of magnetic and gravity sources create fields with one singular point $M(x_0,y_0,z_0)$. In these cases, if a CPS $C(a,b,c)$ coincides with the singular point $M(x_0,y_0,z_0)$, and $n$ is equal to the degree of homogeneity of the anomalous field, then $D(P')$ becomes zero at all points $P'(x',y',z')$ (Stavrev, 1997). Thus, the position of the source point $M$ and the source shape, indicated by the degree $n = -N$ ($N$ is structural index, introduced by Thompson [1982]), can be recognized by a vanishing FDST function (see Stavrev et al., 2006).

The observed field $F$ usually contains a local anomaly $A$ and a background $B$, i.e., $F = A + B$. Within $A$, the background $B$ can be a constant or a linear field: $B(x,y,z) = \ell + ux + vy + wz$. The FDST operator (equation 5) is a linear operator; hence,

$$D_F(x',y',z') = D_A(x',y',z') + D_B(x',y',z'), \quad (6)$$

where $D_F$ is the FDST of $F$, $D_A$ is the FDST of $A$, and $D_B$ is the FDST of the linear $B$. The term $D_B(x',y',z')$ remains a linear function of the observation-point coordinates.

If a CPS $C(a,b,c)$ coincides with the singular point $M(x_0,y_0,z_0)$ of an anomaly $A$, then $D_A(x',y',z') \equiv 0$, and $D_F(x',y',z')$ takes the form of a planar surface $D_B(x',y',z')$. Thus, the inversion of $A$ in the presence of a linear $B$ is implemented by a search for the CPS position and the degree $n$ that flattens out the FDST of $F$. When the data include a linear background, then the background of the upward-continued field also will be linear.

Along with the systematic noise from the deviations of the data from the accepted interpretational model accounted for by MaGSoundFDST, the observed field $F$ may contain random noise. If the sum of the systematic and the random noise is denoted by $O(x,y,z)$, then $F = A + B + O$ and

$$D_F(x',y',z') = D_A(x',y',z') + D_B(x',y',z') + D_O(x',y',z'). \tag{7}$$

The influence of random noise on the estimates is inherently decreased by the use of upward continuation in the FDST. The FDST of measured fields does not include field derivatives, but it can be applied to any data set of calculated or measured derivatives for the respective degree of homogeneity.

## Estimating the linearity of the FDST function

Estimating the linearity of the FDST function is analogous to estimating the linearity of the DST as described in MaGSoundDST (Gerovska et al., 2010). The linearity of an FDST surface $D$ along the observation points within a window $W$ (Figure 1) is assessed by the residual dispersion after a linear regression:

$$q_D^2(a,b,c;n) = (j-1)\sigma_D^2(1-K^2). \tag{8}$$

Here, $j$ is the number of observation points, $\sigma_D^2$ is the dispersion, and $K$ is the generalization of the correlation coefficient of the $D$ surface to the 3D case:

$$K = \frac{1}{(j-1)\sigma_D\sigma_x\sigma_y}\sum_{i=1}^{j}(D_i - D_{\text{ave}})(x_i' - x_{\text{ave}}')$$

$$\times (y_i' - y_{\text{ave}}'), \quad \sigma_D^2 = \frac{1}{j-1}\sum_{i=1}^{j}(D_i - D_{\text{ave}})^2.$$

The values $D_{\text{ave}}$, $x_{\text{ave}}'$, and $y_{\text{ave}}'$ are the average values of the $D$ function and of the $x'$- and $y'$-coordinates in the frame of the window $W'$ at the continuation level $z' = h$ (see Figure 1) and where $\sigma_x^2 = (1/(j-1)) \times \Sigma_{i=1}^{j}(x_i' - x_{\text{ave}}')^2$ (similarly for $\sigma_y^2$).

The estimator $q_D$ gives the minimal deviation of the FDST function $D$ from its linear approximation in the frame of $W'$. When $q_D = 0$ for $W$, then $D_F(x',y',z')$ is a linear function of the horizontal coordinates. In the presence of noise, $q_D$ has a nonzero minimum, reflecting the residual standard deviation of the random noise $O$. The estimator of linearity $q_D$ can be normalized by the residual standard deviation $q_F$ of the anomaly $F$. Thus, the corresponding normalized relative standard deviation $Q$ is

$$Q(a,b,c;N) = \frac{q_D(a,b,c;N)}{q_F}. \tag{9}$$

The $q_F$ in equation 9 is calculated by

$$q_F^2 = \frac{1}{j-1}\sum_{i=1}^{j}(F_i' - F_{\text{ave}}')^2, \tag{10}$$

where $F_{\text{ave}}'$ is the average value of the upward-continued data $F'$ in $W'$.

A smaller value of $Q$ corresponds to a more linear FDST function. The normalized estimator $Q$ attains small values around the extreme points of the anomalous field near the horizontal position of the source's singular point, where $q_F$ has high values and $q_D$ has small values because $D_F(x',y',z')$ is close to zero. The estimator $Q$ increases with distance from the singular point; where the value of $q_D$ is high, the anomalous field intensity is small and the standard deviation $q_F$ is also small. Thus, the distribution of $Q$ facilitates the selection of reliable results from the inversion procedure.

## Implementing the interpretation method

MaGSoundFDST probes the half-space under the observations for a series of assumed structural indices $N$ using a moving window $W$ to produce the FDST estimator-of-linearity measure field $Q(a,b,c;N)$. The procedure closely follows that of MaGSoundDST (Gerovska et al., 2010). Three maps are compiled from the 3D functions $Q(a,b,c;N)$. We compile a 2D map $Q(Q_{\text{min}})$ that combines all subsets of 3D functions $Q(a,b,c;N)$ into a 2D function by obtaining one $Q_{\text{min}}$ value for each vertical probing line at each horizontal location $(a,b)$. The local minima of the $Q(Q_{\text{min}})$ map determine the horizontal positions of the sources. The values of $N$ and the CPS depth $c$ corresponding to each local minimum of the $Q(Q_{\text{min}})$ map give the structural index and depth of the sources, mapped as $N(Q_{\text{min}})$ and $Z(Q_{\text{min}})$, respectively.

MaGSoundFDST requires several inputs: the CPS grid, moving window size, height of the upward continuation, and a set of structural indices. The CPS grid spacing and the number of probe points along the vertical line under each window center $(a,b)$ should cover the anticipated depths of the sources. To detect the sources, the size of the window in the two horizontal directions needs to be at least

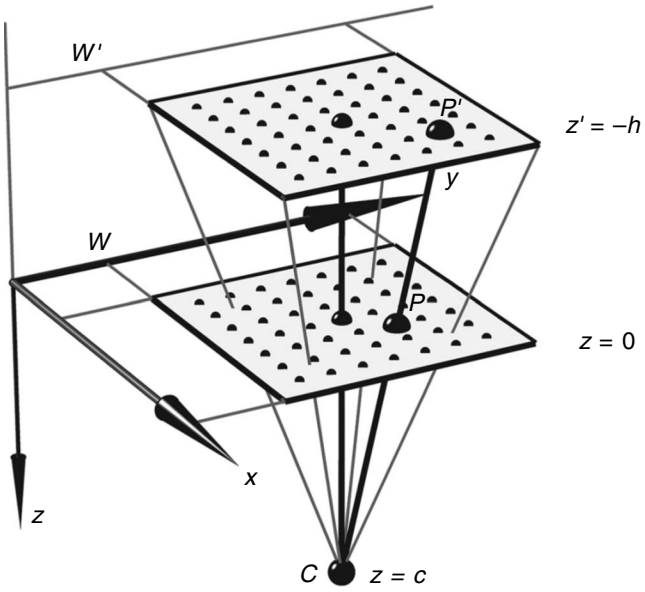


Figure 1. Similarity transformation of the data in the window $W$ at level $z = 0$ to the upward-continuation level at $z' = -h$ from a probe CPS $C$ at depth $z = c$. The similarity transform $A'$ at level $z'$ is equal to the value of the anomaly $A$ in the intermediate point $P$, multiplied by $t^n$ according to equation 4. The coefficient of similarity is $t = CP'/CP$, where $CP'$ and $CP$ are the distances between the point $C$ and points $P'$ and $P$, respectively. The field $A$ at $P$ is obtained through spline interpolation of the data at the original grid points.

twice the estimated depth to the sources. Window sizes can be varied to find the optimal value, taking into account the main wavelength of the inverted anomaly or set of anomalies. Currently, MaGSoundFDST uses a constant window size for all CPS, but it could be improved through an adaptive window, i.e., by increasing the window size with deeper CPS. The height of the upward continuation $h$, i.e., the level at which the FDST $D$ is calculated, should be near or less than half of the depth to the supposed sources (Stavrev et al., 2006). The set of structural indices are integers or nonintegers (to account for finite dimensions of the sources) between 0 and 3 for magnetic anomalies and $-1$ and 2 for gravity anomalies. Non-integer structural indices within these ranges will give better resolution of the estimates from the inversion.

Once the parameters are selected, MaGSoundFDST calculates the upward-continued field, $A(x',y',z')$, at a height $h$ over the whole data grid in the frequency domain using the transfer function $V(k_x,k_y) = e^{-h|k|}$, where $k = (k_x^2 + k_y^2)^{1/2}$ and where $k_x$ and $k_y$ are wavenumbers in the $x$- and $y$-directions, respectively (Blakely, 1995).

Next, MaGSoundFDST starts working in a window mode. The similarity transform $A'(x',y';N)$ is obtained for each $W'$ with center $(a,b)$ (see Figure 1). The value $A'(x',y')$ depends on the choice of the central points of similarity, which are distributed along the vertical line through the window's center and serve as probe points in estimating the FDST for the different $n = -N$. The direct similarity transform $A'$ at the regular grid point $P'$ is equal to the value of the interpolated anomaly $A$ at the intermediate point $P$, multiplied by $t^n$, according to equation 4. In this case, the coefficient of similarity is $t = CP'/CP$, where $CP'$ and $CP$ are the distances between the probe point $C$ and the points $P'$ and $P$, respectively (see Figure 1). Once $A'(x',y';N)$ is available, the FDST $D(x',y';N)$ within $W'$ is obtained using equation 5. The estimator of linearity $Q(a,b,c;N)$ of $D(x',y';N)$ is then calculated, following equations 8–10.

From the series of 3D functions $Q(a,b,c;N)$, MaGSoundFDST compiles a $Q(Q_{\min})(x,y)$ map by finding each minimum (only in the vertical direction) of $Q(a,b,c;N)$ at each horizontal position $(a,b)$ for all structural indices $N$ and all depths $c$. That is, $Q(Q_{\min})(x,y)$ is a map of $Q_{\min} = Q_{\min}(a,b) = \min_{c,N} Q(a,b,c;N)$ (see Gerovska et al., 2010). Then the local minima $Q(Q_{\min})_{\min}$ of the $Q(Q_{\min})$ map are estimated. A $Q_{\min}$ is accepted if it is less than one, i.e., the residual standard deviation $q_D$ of the FDST is smaller than the residual standard deviation $q_F$ of the original field because the FDST should be flatter than the original anomaly (see equation 9). This acceptance level could be set lower to accept only the most precise, best-constrained estimates. The minima of the $Q(Q_{\min})$ determine the horizontal positions of singular points of the sources. The patterns of the anomalies of the $Q(Q_{\min})$ map may help define the shape of the horizontal projections of complex sources such as intrusive sills, effusive flows, tubes, and veins.

MaGSoundFDST applies a refinement procedure, proposed in Gerovska et al. (2010), and obtains solutions at any point in $R^3$, as opposed to the discrete minima defined by the CPS grid positions. The refinement involves interpolating a best-fitting ellipsoid of constant $Q$ from the $Q$ values of all one-point-radius, nearest-CPS-grid neighbors from the 3D function $Q(N)$ to which the discrete solution belongs. The center of such an ellipsoid defines the refined source location. The coordinates of these new refined $Q$ minima are the estimated locations of the simple sources.

Optionally, MaGSoundFDST produces two additional maps, $N(Q_{\min})$ and $Z(Q_{\min})$, which may help determine the horizontal shapes of sources (for details, see Gerovska et al., 2010) but are not always necessary. The $N(Q_{\min})$ and $Z(Q_{\min})$ maps are obtained by finding the structural index and the CPS depth corresponding to each value of the $Q(Q_{\min})$ map.

As another option, MaGSoundFDST can automatically eliminate those minima of $Q(Q_{\min})$ that coincide with points of the $(a,b)$ probing set where the windows encompass a field with low gradient. Inversion using data in such windows is unstable and the results are unreliable. Recognizing such points $(a,b)$ is based on the value of $q_F$ in $W$ with the center at $(a,b)$. If $q_F$ is less than a threshold $(q_F)_{\min}$ (determined by testing), then the minimum of $Q(Q_{\min})$ at $(a,b)$ should be rejected. We find a suitable $(q_F)_{\min}$ to be 75% of the maximum $(q_F)_{\max}$ of $q_F$. Note that $q_F$ is window-size and field-gradient dependent (Gerovska et al., 2010).

## RESULTS

### Model tests

We applied MaGSoundFDST to three different model data sets to demonstrate different features of the technique. The first example is the field of a magnetized sphere whose center does not coincide with a CPS grid point. This shows that MaGSoundFDST works successfully on magnetic field data, is robust to random noise, and can estimate source coordinates correctly using the refinement option. The second simple example, inverting the gravity field of a spherical mass, demonstrates that MaGSoundFDST works well with gravity data from simple sources in the presence of a linear background. The third example is the inversion of magnetic data from five sources with interfering fields. It demonstrates how each singular point is predicted by a unique estimate and shows the influence of the upward-continuation height on the solution resolution.

The first example is a noise-corrupted magnetic model data set of $40 \times 38$ points, generated by a spherical source with its center at $(x_0 = 4.85, y_0 = 4.65, z_0 = 0.85)$ km and having an induced magnetization with an inclination of 45° and declination of 0°. The CPS $(a,b,c)$ set has a 3D grid spacing of $0.25 \times 0.25 \times 0.25$ km and six vertical probing points. The moving window size is $21 \times 21$ points ($5 \times 5$ km). The threshold value for $q_F$ was 980 nT, which is 75% of $(q_F)_{\max}$. The upward-continuation height $h$ is 0.3 km.

We contaminated the source field $A$ with zero-mean Gaussian distributed random noise in the 10–15-dB signal-to-noise ratio (S/N) range $[S/N = 10 \log_{10}(\sigma_{\text{anomaly}}/\sigma_{\text{noise}})]$, where $\sigma$ denotes standard deviation in 1-dB increments. We simulated 100 replicates for each S/N; the statistics of the perturbations of $Q(Q_{\min})_{\min}$ and its respective parameters $(a,b,c,N)$ determined by MaGSoundFDST are presented in Table 1. The perturbation analysis shows that MaGSoundFDST is robust for S/N as low as 10 dB. We have also performed noise analysis with the MaGSoundDST method (Gerovska et al., 2010) for the same S/N range and the same replicates as for MaGSoundFDST; the results are presented in Table 2. The comparison between Tables 1 and 2 shows the better response to random noise of MaGSoundFDST when estimating the depth and structural index of the spherical source. MaGSoundDST performs better at determining the source's horizontal position because the FDST calculation involves upward analytical continuation, whereas the DST calculation involves horizontal derivatives. Thus, the two methods respond differently to random noise.

**Table 1. Results from the noise analysis for the spherical-magnetic-source ($x_0 = 4.85, y_0 = 4.65, z_0 = 0.85$ km) case for MaGSoundFDST. Mean $\mu$ and standard deviation $\sigma$ of $Q(Q_{min})_{min}$ and the respective estimated parameters $a$, $b$, $c$, and $N$ for different S/N noise-contaminated signals based on 100 noise replicates per S/N.**

| S/N (dB) | $(Q(Q_{min}))_{min}$ | | $a$ (km) | | $b$ (km) | | $c$ (km) | | $N$ | |
|---|---|---|---|---|---|---|---|---|---|---|
| | $\mu$ | $\sigma$ | $\mu$ | $\sigma$ | $\mu$ | $\sigma$ | $\mu$ | $\sigma$ | $\mu$ | $\sigma$ |
| 10 | 0.06 | 0.06 | 4.68 | 0.28 | 5.00 | 2.00 | 0.69 | 0.21 | 2.36 | 0.94 |
| 11 | 0.04 | 0.06 | 4.73 | 0.26 | 4.87 | 1.46 | 0.74 | 0.18 | 2.57 | 0.82 |
| 12 | 0.03 | 0.04 | 4.79 | 0.19 | 4.87 | 1.08 | 0.79 | 0.13 | 2.77 | 0.64 |
| 13 | 0.02 | 0.03 | 4.82 | 0.12 | 4.75 | 0.72 | 0.82 | 0.07 | 2.92 | 0.39 |
| 14 | 0.01 | 0.01 | 4.84 | 0.07 | 4.71 | 0.59 | 0.84 | 0.02 | 2.98 | 0.20 |
| 15 | 0.01 | 0.00 | 4.85 | 0.01 | 4.64 | 0.01 | 0.85 | 0.00 | 3.00 | 0.00 |

**Table 2. Results from the noise analysis for the spherical-magnetic-source ($x_0 = 4.85, y_0 = 4.65, z_0 = 0.85$ km) case for MaGSoundDST. Mean $\mu$ and standard deviation $\sigma$ of $Q(Q_{min})_{min}$ and the respective estimated parameters $a$, $b$, $c$, and $N$ for different S/N noise-contaminated signals as in Table 1, based on 100 noise replicates per S/N.**

| S/N (dB) | $Q(Q_{min})_{min}$ | | $a$ (km) | | $b$ (km) | | $c$ (km) | | $N$ | |
|---|---|---|---|---|---|---|---|---|---|---|
| | $\mu$ | $\sigma$ | $\mu$ | $\sigma$ | $\mu$ | $\sigma$ | $\mu$ | $\sigma$ | $\mu$ | $\sigma$ |
| 10 | 0.93 | 0.03 | 4.85 | 0.02 | 4.65 | 0.02 | 0.50 | 0.01 | 2.00 | 0.00 |
| 11 | 0.86 | 0.03 | 4.85 | 0.01 | 4.65 | 0.02 | 0.54 | 0.10 | 2.11 | 0.31 |
| 12 | 0.80 | 0.02 | 4.85 | 0.01 | 4.65 | 0.02 | 0.64 | 0.16 | 2.42 | 0.50 |
| 13 | 0.73 | 0.02 | 4.85 | 0.01 | 4.65 | 0.02 | 0.79 | 0.11 | 2.86 | 0.35 |
| 14 | 0.68 | 0.02 | 4.86 | 0.01 | 4.65 | 0.01 | 0.83 | 0.06 | 2.97 | 0.17 |
| 15 | 0.63 | 0.02 | 4.85 | 0.01 | 4.65 | 0.02 | 0.84 | 0.01 | 3.00 | 0.00 |

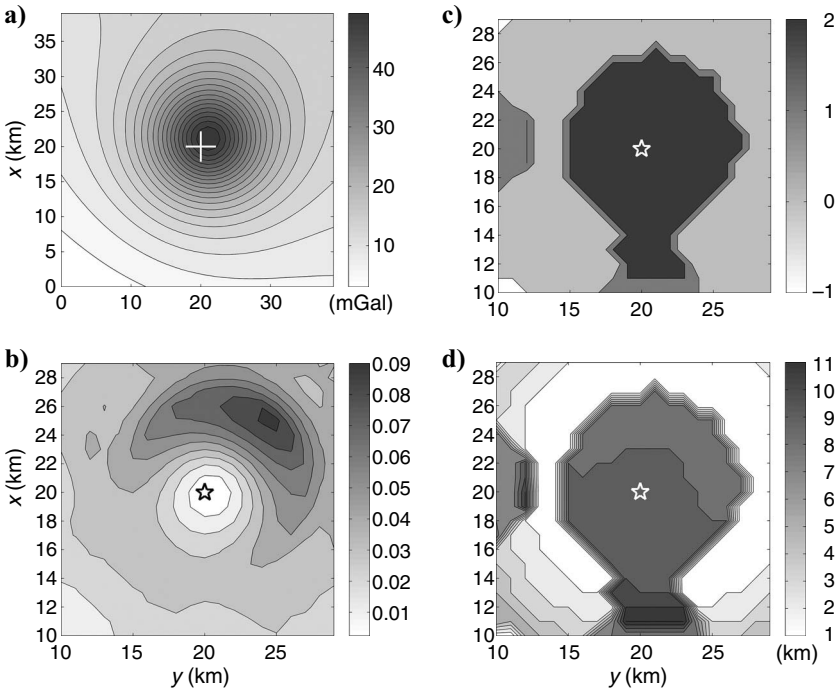


Figure 2. Model gravity data set caused by a sphere (point mass) and linear background, and MaGSoundFDST results. (a) Gravity field $F = A + B$, where $A$ is the field of the sphere with a center at (20, 20, 9) km, marked with a cross, and $B = 2 + 0.1x + 0.2y$ is the linear background. (b) $Q(Q_{min})$. (c) $N(Q_{min})$. (d) $Z(Q_{min})$. The estimates for the source's horizontal location are marked with open stars ($N = 2$).

The second model example is a gravity data set caused by a spherical source (Figure 2a) with its center at ($x_0 = 20$, $y_0 = 20$, $z_0 = 9$) km, having a 5-km radius and a 1-g/cm$^3$ density contrast. The input data grid is sized as $40 \times 40$ points ($40 \times 40$ km). A linear background $B = 2 + 0.1x + 0.2y$ has been added to the source anomaly. We applied MaGSoundFDST with a window size of $21 \times 21$ points ($20 \times 20$ km). The CPS grid has a 3D grid spacing of $1 \times 1 \times 1$ km and 15 vertical probe points. For an upward-continuation height $h = 2$ km, MaGSoundFDST returns the correct horizontal position (20,20) km, depth 9 km, and structural index two for $Q(Q_{\min})_{\min} = 0.0024$. The maps $Q(Q_{\min})$, $N(Q_{\min})$, and $Z(Q_{\min})$ for the set of structural indices tested ($N = -1$, 0, 1, and 2) are given in Figure 2b-d.

The third model example is the inversion of synthetic data generated by five magnetic bodies with fields interfering somewhat to produce a linear or nonlinear background within certain windows. This is the same model used to test the Euler deconvolution method based on the DST by Gerovska and Araúzo-Bravo (2003) and MaGSoundDST by Gerovska et al. (2010). The five bodies comprise two spheres, a sill, a vertical dike, and a pipe, characterized by 10 singular points (Figure 3a, Table 3).

The input data grid measures $150 \times 150$ points. MaGSoundFDST was applied for a CPS ($a$,$b$,$c$) set with a 3D grid spacing of $0.25 \times 0.25 \times 0.1$ km, a window measuring $11 \times 11$ points ($2.5 \times 2.5$ km), and 40 vertical probe points. Three upward-continuation heights $h$ were used: 0.12, 0.25, and 0.5 km. The continuation height 0.25 km, which proved to be the most suitable to estimate the parameters of the simple sources correctly, produced 10 solutions. The coordinates and structural indices of the spheres, pipe, and vertical dike were estimated correctly, with two additional solutions for the pipe and the dike. The two singular points detected for the sill model S2 are indicated by the numbers 1 and 4 in Figure 3a.

This model example confirms the results of the 2D case study (Stavrev et al., 2006), which recommends a continuation height less than half the depth to the sources. In the five-body case, the depth to top of the shallowest sources S2 and S3 is 1 km; hence, an $h$ of 0.5 km or smaller should be suitable. A height of 0.12 km leads to too many estimates, and 0.5 km leads to too few. An upward-continuation height of 0.5 km detects only singular point 4 of the sill, whereas $h = 0.12$ km detects three of its singular points (1, 2, and 4), but 1 and 2 have incorrect structural indices ($N = 2$ instead of 1) (see Table 3).

Maps $Q(Q_{\min})$, $N(Q_{\min})$ and $Z(Q_{\min})$ for an upward-continuation height of 0.25 km are shown in Figure 3b-d. Two of the singular points of source S2 are not detected with minima of $Q(Q_{\min})$ because of the proximity of the other two singular points and of the dike. The accuracy of the estimate is similar to that of the Euler deconvolution procedure based on the DST (Gerovska and Araúzo-Bravo, 2003) and to that of MaGSoundDST (Gerovska et al., 2010). An advantage over the DST-based Euler deconvolution procedure is that here we avoid the process of reducing many spurious solutions to one estimate corresponding to each source.

## Bishop test data set

The complex Bishop 3D basement model provides magnetic data sets that test new inversion techniques and compare their performance (Reid et al., 2005; Williams et al., 2005; Salem et al., 2008; Fedi et al., 2009). The realistic basement model is derived from real topographic data for a portion of the volcanic tablelands area north of Bishop, California, U.S.A. The topography has been upscaled by a factor of 30 in three dimensions and then shifted in depth such that the structures are below the surface with depths of approximately 0.1–9.3 km. This topographic surface forms the top of a magnetic basement layer. Various depths to the base of the magnetic layer have been used to approximate a passive margin setting (G. Flanagan, personal communication, 2009). The magnetic field was calculated for each model using various values for the inclination and a total geomagnetic field of 50,000 nT. Williams et al. (2002, 2005) use the magnetic response of a basement with constant magnetic susceptibility in their study on the performance of grid Euler deconvolution with and without 2D constraints. Reid et al. (2005) and Fedi et al.

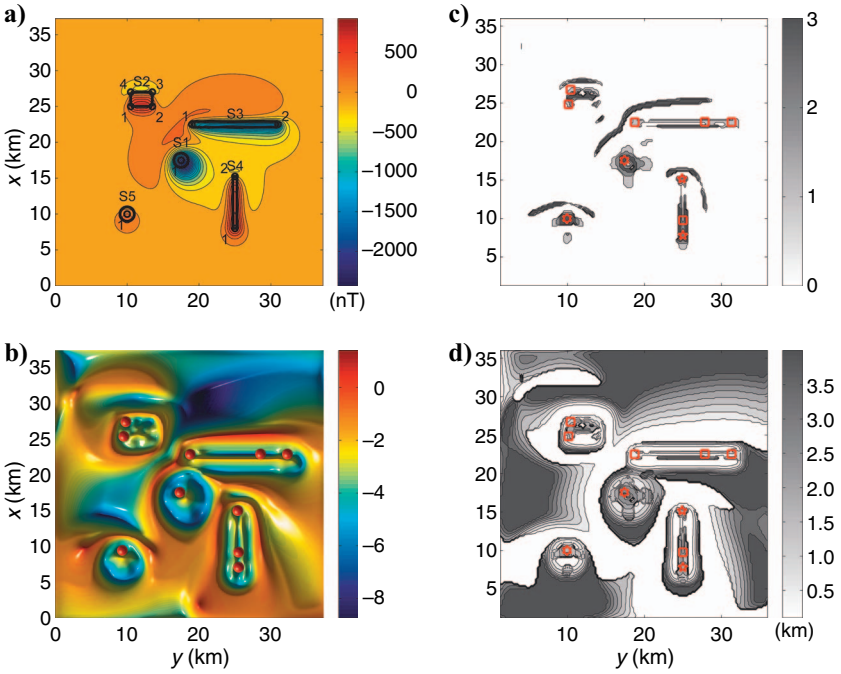


Figure 3. Model magnetic data set caused by five bodies: S1 and S5 (spheres), S2 (sill), S3 (vertical dike), and S4 (pipe). (a) Anomalous magnetic field; (b) $Q(Q_{\min})$ on a logarithmic scale; (c) $N(Q_{\min})$; (d) $Z(Q_{\min})$. The inversion uses an upward-continuation height $h$ of 0.25 km and window size of $11 \times 11$ grid points ($2.5 \times 2.5$ km). The lower half-space is probed up to a depth of 4 km along 40 points. The estimated singular-point structural indices are marked in (b) with red spheres and in (c) and (d) with red squares ($N = 1$), stars ($N = 2$), and hexagons ($N = 3$). The estimates with $N = 0$ do not correspond to real sources and are automatically filtered out.

**Table 3. Real ($x_0$,$y_0$,$z_0$,$N$) and estimated ($a$,$b$,$c$,$N_{est}$) parameters of the singular points (SP) of the five bodies causing the magnetic anomalies in Figure 3a. The threshold value for $Q$ is one. The heights $h$ of the upward analytical continuation are 0.5, 0.25, and 0.12 km. Dashes mean no solution was obtained for the given source and corresponding height $h$. Asterisks mark locations with no real sources but where a solution was obtained.**

| Source | SP | $x_0$ (km) | | $a$ (km) | | $y_0$ (km) | | $b$ (km) | | $z_0$ (km) | | $c$ (km) | | $N$ | | $N_{est}$ | | $Q(Q_{min})_{min}\times10^4$ | | |
|---|---|---|---|---|---|---|---|---|---|---|---|---|---|---|---|---|---|---|---|---|
| $h$ (km) | | | 0.5 | 0.25 | 0.12 | | 0.5 | 0.25 | 0.12 | | 0.5 | 0.25 | 0.12 | | 0.5 | 0.25 | 0.12 | 0.5 | 0.25 | 0.12 |
| S1 sphere | 1 | 17.5 | 17.6 | 17.6 | 17.6 | 17.5 | 17.4 | 17.4 | 17.4 | 3 | 3.0 | 3.0 | 3.0 | 3 | 3 | 3 | — | 4 | 3 | 2 |
| * | * | * | — | — | 17.3 | * | — | — | 20.7 | * | — | 2.8 | — | * | — | — | 1 | — | — | 31 |
| S2 sill | 1 | 25 | — | 24.8 | 24.9 | 10.5 | | 10.1 | 10.2 | 1 | — | 0.9 | 1.6 | 1 | — | 1 | 2 | — | 184 | 15 |
| | 2 | 25 | — | — | 24.8 | 13.5 | — | — | 13.8 | 1 | — | — | 1.5 | 1 | — | — | 2 | — | — | 192 |
| | 3 | 27 | — | — | — | 13.5 | — | — | — | 1 | — | — | — | 1 | — | — | — | — | — | — |
| | 4 | 27 | 26.7 | 26.7 | 26.7 | 10.5 | 10.4 | 10.4 | 10.4 | 1 | 1.2 | 1.2 | 1.2 | 1 | 1 | 1 | 1 | 40 | 67 | 63 |
| S3 dike | 1 | 22.5 | 22.5 | 22.5 | 22.5 | 19 | 18.8 | 18.7 | 18.7 | 1 | 0.8 | 0.8 | 0.8 | 1 | 1 | 1 | 1 | 5 | 5 | 4 |
| | 2 | 22.5 | 22.5 | 22.5 | 22.5 | 31 | 31.3 | 31.3 | 31.3 | 1 | 0.8 | 0.8 | 0.8 | 1 | 1 | 1 | 1 | 6 | 7 | 5 |
| * | * | * | 22.5 | 22.5 | 22.5 | * | 28.1 | 27.8 | 28.0 | * | 0.8 | 0.8 | 0.8 | * | 1 | 1 | 1 | 5 | 7 | 5 |
| S4 pipe | 1 | 8 | 7.8 | 7.8 | 7.8 | 25 | 25.0 | 25.0 | 25.0 | 1.5 | 1.5 | 1.5 | 1.5 | 2 | 2 | 2 | 2 | 2 | 3 | 3 |
| * | * | * | 9.7 | 9.8 | 9.8 | * | 25.0 | 25.0 | 25.0 | * | 0.9 | 1.0 | 1.0 | * | 1 | 1 | 1 | 24 | 32 | 28 |
| | 2 | 15.25 | 15.2 | 15.2 | 15.2 | 25 | 24.6 | 25.0 | 24.9 | 1.5 | 1.6 | 1.5 | 1.6 | 2 | 2 | 2 | 2 | 22 | 28 | 18 |
| S5 sphere | 1 | 10 | 10.0 | 10.0 | 10.0 | 10 | 9.9 | 9.9 | 9.9 | 2 | 1.9 | 1.9 | 1.9 | 3 | 3 | 3 | 3 | 11 | 12 | 9 |

(2009) use the same depth model but with some arbitrary additional susceptibility boundaries to represent basement lithologic changes or intrusives.

We used the Bishop 5x data set with geomagnetic inclination of 45° and the base of the magnetic basement layer coinciding with the Moho discontinuity (Figure 4a). Forward calculations of the magnetic field were performed using GM-SYS-3D from Northwest Geophysical Associates Inc. (U.S.A.) using default extrapolation parameters. Our test data grid had $670\times634$ points with a spacing of 0.6 km in the two horizontal directions. We did not need to reduce the data to the pole as in Williams et al. (2005) because the results from the MaGSoundFDST procedure were not affected by the magnetization vector direction. The lower half-space was tested along 20 probe points with a spacing of 0.6 km, equal to the grid spacing. We applied a window size of $13\times13$ points ($7.2\times7.2$ km). The height of upward continuation was 0.3 km. The solutions for simple sources and the three maps generated by MaGSoundFDST for structural indices 0, 0.5, 1, and 2 (no solutions obtained for $N=3$) clearly outline the boundaries of seven basement areas with different magnetic susceptibilities (Figures 4b-d and 5). Also outlined are vertical boundaries between the basement and the sedimentary cover, i.e., contrasts resulting from the basement relief.

Figure 6a presents the residuals between the estimated and the true depths to the top of basement versus the true basement depths. A group of residuals, those with the highest positive values corresponding to each true depth, form a line (marked in red in Figure 6a) that corresponds to a group of solutions with depth equal to or near 12 km, the maximum depth covered by the CPS grid. We attribute these solutions to a boundary effect and exclude them from further analysis using the MaGSoundFDST option as a filter.

We continue our analysis with only the out-of-the-line 460 solutions. The solution residuals (Figure 6a) show variability in relation to the true top of the magnetic basement depths (Figure 5). Usually we associate magnetic susceptibility contacts and step structures with structural indices 0 and 0.5. In the Bishop model's magnetic data case, a comparable number of solutions with $N=0$ have residuals within the range $[-2,2]$ km and outside this range. Almost all of the solutions with $N=0.5$ are within the range $[-2,2]$ km, which in the Bishop model's example proves them most reliable as an estimate of the depth to the top of the magnetic basement. Williams et al. (2005) pick out a structural index of 0.5 as the optimum single value to get the best average fit to the Bishop model data using their choice of Euler deconvolution algorithm. But that particular algorithm requires an a priori assumption of the structural index, and the error histogram is very wide. It is well known in practice with real geology that if an $N$ value must be assumed, 0.5 gives the best overall fit with simple Euler deconvolution — but it is a very broad best fit. With MaGSoundFDST, we derive the best structural index, feature by feature.

Confronted with the wide range of residual values for a structural index of zero, we took a closer look at the relief of the Moho discontinuity (Figure 7a). Over the Bishop model's area, the Moho discontinuity approximates roughly a plain dipping north-northwest; thus, it is generally deeper in the areas where the depth to the top of the basement is small and shallower where the depth to the basement top is large. We found a relation between the regression line of the residuals of the solutions produced by MaGSoundFDST and the regression

line of the Moho discontinuity depth versus the depth to top of basement (Figure 7b). The slopes of the two regression lines are similar, −0.8 and −0.7, which shows that MaGSoundFDST is somewhat sensitive to the depth to the Moho.

We applied Euler deconvolution with an unprescribed structural index (Gerovska and Araúzo-Bravo, 2003) to the same data set using the same window size as in MaGSoundFDST, acceptance parameter 0.00005 and no clustering. For this strict acceptance parameter, we obtained 4830 solutions with a structural index between 0 and 2.12, mean of 0.1, and standard deviation of 0.1. The residuals between the estimated and true depths to the basement from the DST-based Euler deconvolution are shown in Figure 6b. The DST-Euler method residuals show similar variability to those of the MaGSoundFDST method (Figure 6a). When comparing the solution residuals of the DST-based Euler method without clustering and those of the MaGSoundFDST, we should note that a group of solutions of the DST-based Euler method without clustering represents one simple source. In contrast, MaGSoundFDST produces one solution per detected source. In geologic settings similar to the Bishop model, the two procedures can complement each other because the DST-Euler solutions are of a more statistical, generalized character, whereas MaGSoundFDST is more definitive in determining the source depth and structural index in relation to the estimated source's horizontal location.

## Bolyarovo-Voden magnetic anomaly, southeast Bulgaria

The Strandza intrusive zone in southeast Bulgaria outcrops south of the Burgas volcano-plutonic zone amid the Late Cretaceous complexes of the Strandza and Sakar Mountains. It is 150 km long west-northwest–east-southeast and 35 km wide. The intrusive bodies are concentrated in three subzones parallel to the main faults in the Strandza Mountains. The predominant direction of the magnetic anomaly axes is west-northwest–east-southeast and rarely, north-northeast–south-southeast. These directions coincide with the main fault structures that have controlled magmatic processes in the zone.

The Bolyarovo-Voden magnetic anomalous zone, which we chose for MaGSoundFDST analysis, is a magnetic manifestation of part of the Strandza intrusive zone and covers three almost parallel rows of anomalies: Bolyarovo in the north, Voden in the middle, and Sharkovo in the south (Figure 8a and b). The Voden anomaly is

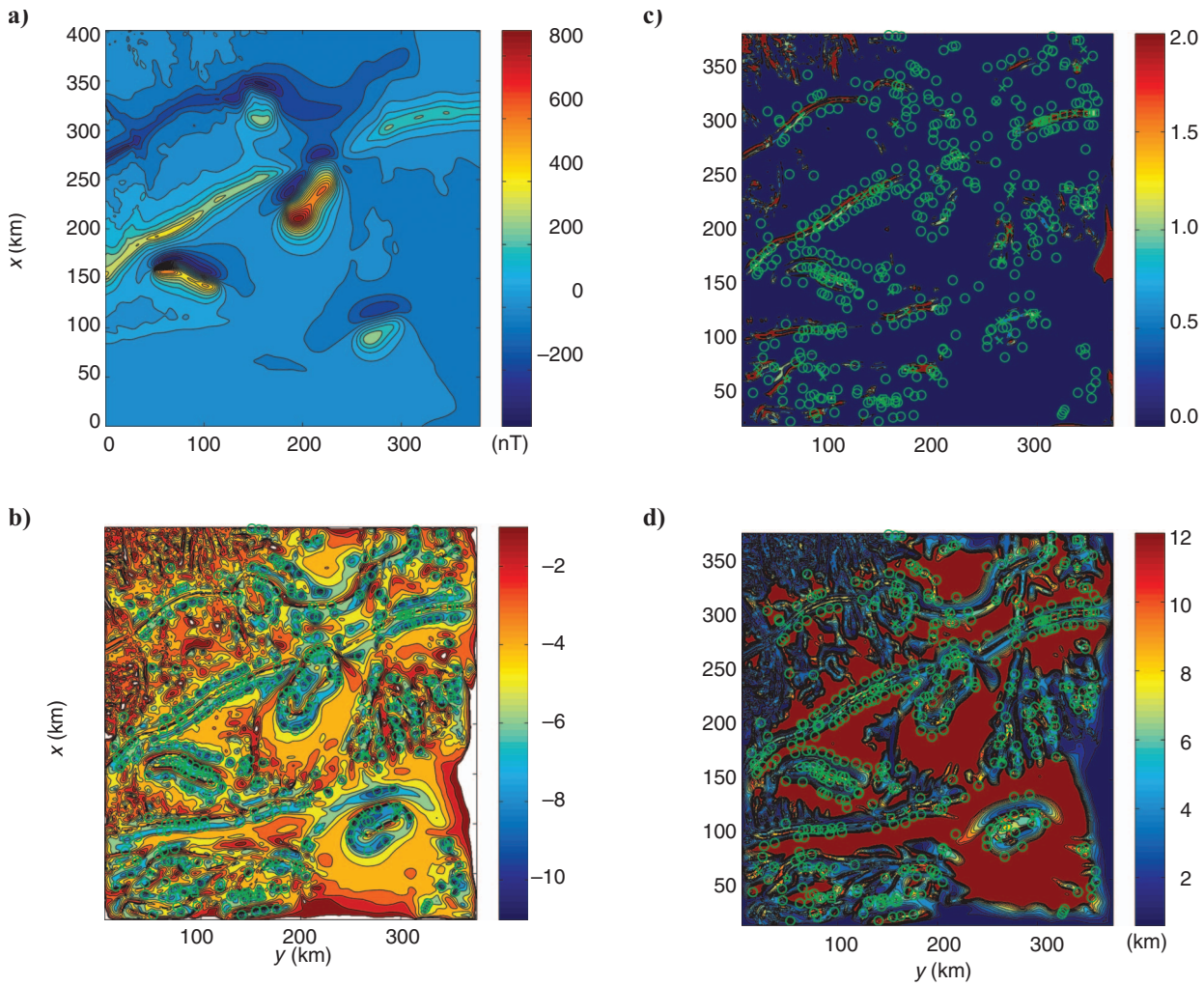


Figure 4. (a) Bishop model's total magnetic anomaly data and MaGSoundFDST inversion results. (b) $Q(Q_{min})$ on a logarithmic scale, $Q(Q_{min})>0.001$ in the white areas. (c) $N(Q_{min})$. (d) $Z(Q_{min})$. The accepted estimates with a threshold of $Q(Q_{min})_{min} = 0.001$ are marked with green circles ($N = 0$), crosses ($N = 0.5$), squares ($N = 1$), and pentagons ($N = 2$).

weakly manifested in the interference strip between the more intense neighboring anomalies, of which Sharkovo reaches 3000 nT (Figure 8a). The Bolyarovo series of anomalies has lower mean intensity (>1000 nT) but is wider. The minima of the three anomalies accompanying the anomalous maxima are in the northern direction, indicative of normal magnetization of the disturbing bodies. The three anomalous zones of different amplitudes can be distinguished easily on the magnitude magnetic anomaly map on logarithmic scale (Stavrev and Gerovska, 2000; Gerovska and Araúzo-Bravo, 2006). Stavrev and Raditchev (1998) performed 2.5D modeling on the three anomalies (Figures 8a and f). They deduced that the upper sur-

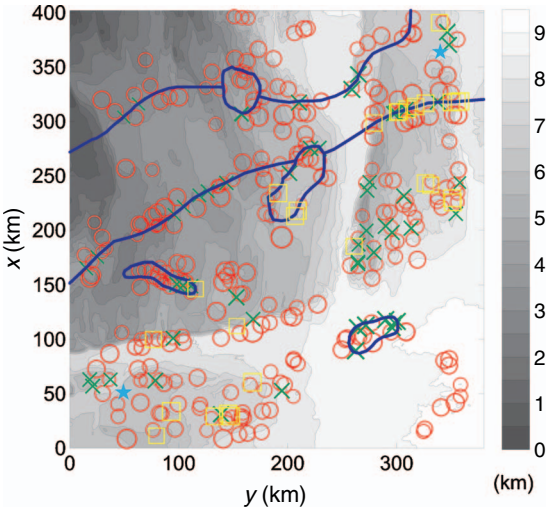


Figure 5. MaGSoundFDST estimates for the source locations marked with red circles ($N = 0$), green crosses ($N = 0.5$), yellow squares ($N = 1$), and turquoise stars ($N = 2$), size proportional to the source depth. The symbols are underlain by a contour map of the topography of the basement from the Bishop model (in grayscale) and by the outlines of the regions with different magnetic susceptibility (in dark blue).

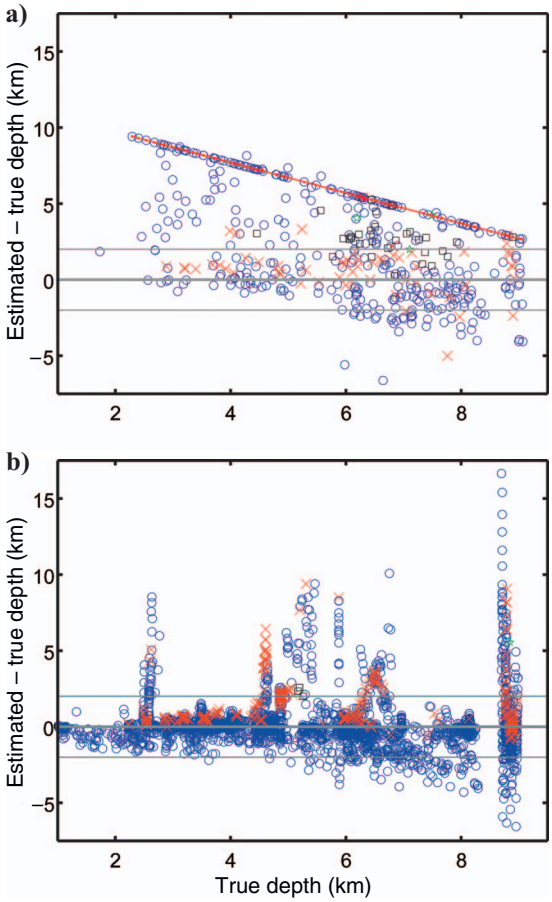


Figure 6. Residuals between the estimated and true depth-to-basement versus the true depth-to-basement: (a) MaGSoundFDST. Results for different structural indices are marked with blue circles ($N = 0$), red crosses ($N = 0.5$), black squares ($N = 1$), and green stars ($N = 2$). (b) DST-based Euler. The results are marked with blue circles ($N < 0.25$), red crosses ($0.25 \le N < 0.75$), black squares ($0.75 \le N < 1.5$), and green stars ($N \ge 1.5$).

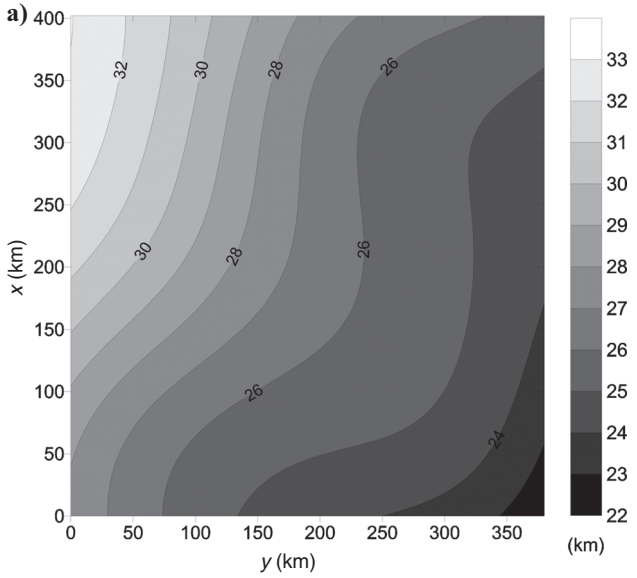


Figure 7. (a) Depth to the Moho discontinuity for the Bishop model. (b) Regression lines through the Moho discontinuity depth versus the depth to top of basement (true depth) and through the residuals between the estimated and the true depth to basement versus the true depth to basement for the MaGSoundFDST estimates for the Bishop 5x model.

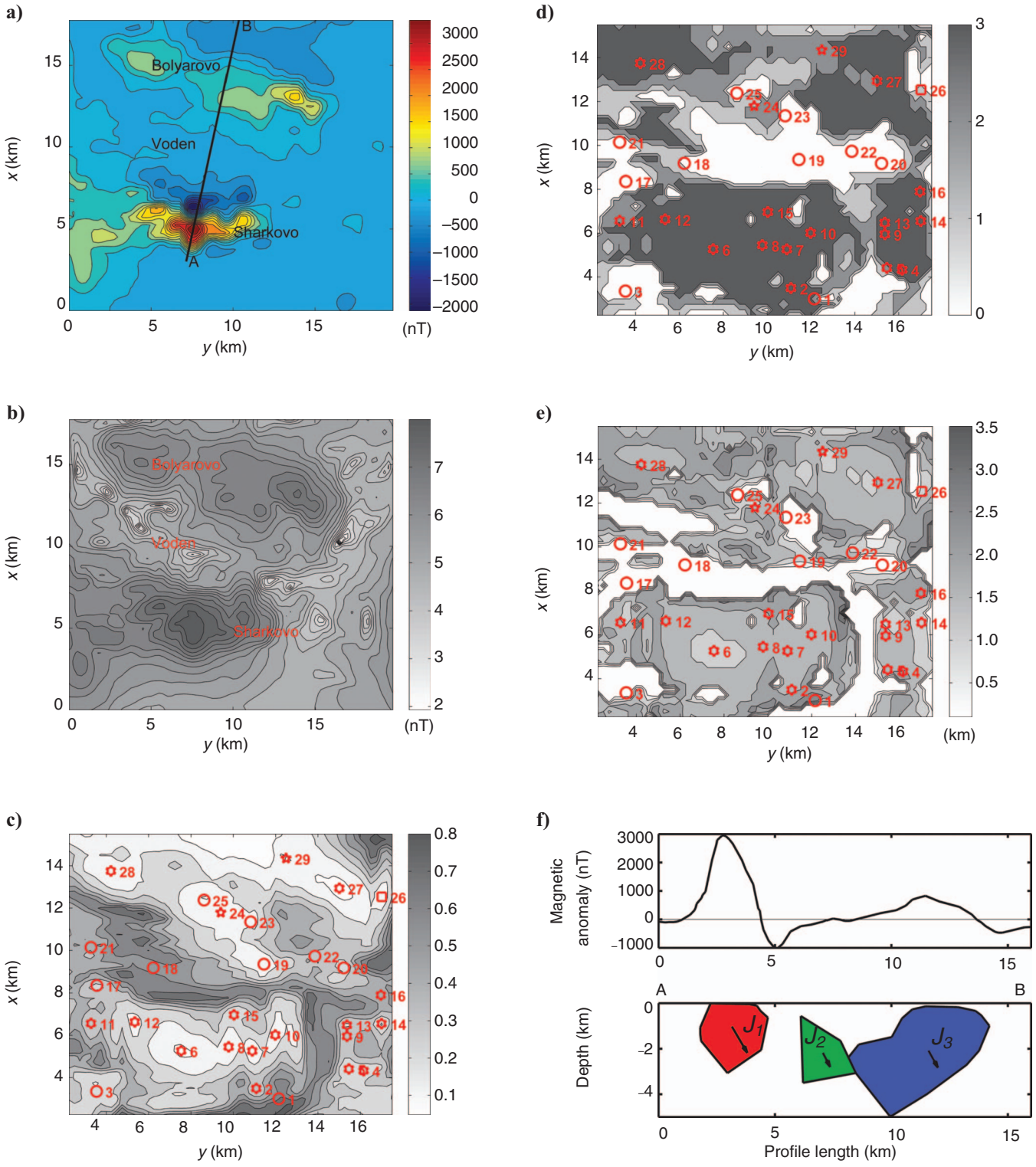


Figure 8. Bolyarovo-Voden magnetic anomaly, southeast Bulgaria, and MaGSoundFDST results. (a) Anomalous vertical magnetic component field. (b) Magnitude magnetic anomaly (Gerovska and Araúzo-Bravo, 2006) on a logarithmic scale. (c) $Q(Q_{min})$. (d) $N(Q_{min})$. (e) $Z(Q_{min})$. The estimated source structural indices are marked in by red squares ($N = 1$), stars ($N = 2$), and hexagons ($N = 3$) with numbers corresponding to the sources in Table 4. (f) Results from 2.5D magnetic modeling of profile A–B in (a) (after Stavrev and Raditchev, 1998).

**Table 4. Estimated parameters $a$, $b$, $c$, and $N_{est}$ of magnetic field sources causing the Bolyarovo-Voden anomaly, southeast Bulgaria. The source numbers correspond to those in Figure 8c-e.**

| Source number | $N$ | $a$ (km) | $b$ (km) | $c$ (km) | $(Q(Q_{min}))_{min}$ |
|---|---|---|---|---|---|
| 1 | 0 | 3.0 | 12.2 | 0.2 | 0.18 |
| 2 | 3 | 3.5 | 11.1 | 1.9 | 0.32 |
| 3 | 0 | 3.4 | 3.5 | 1.0 | 0.19 |
| 4 | 3 | 4.3 | 16.2 | 2.0 | 0.24 |
| 5 | 3 | 4.4 | 15.5 | 1.9 | 0.20 |
| 6 | 3 | 5.3 | 7.5 | 1.4 | 0.09 |
| 7 | 3 | 5.3 | 10.9 | 1.6 | 0.16 |
| 8 | 3 | 5.5 | 9.8 | 1.7 | 0.12 |
| 9 | 3 | 6.0 | 15.4 | 1.7 | 0.31 |
| 10 | 3 | 6.0 | 12.0 | 1.6 | 0.14 |
| 11 | 3 | 6.6 | 3.3 | 1.8 | 0.32 |
| 12 | 3 | 6.6 | 5.4 | 1.8 | 0.18 |
| 13 | 3 | 6.5 | 15.4 | 1.5 | 0.28 |
| 14 | 3 | 6.6 | 17.0 | 1.2 | 0.19 |
| 15 | 3 | 7.0 | 10.0 | 2.1 | 0.21 |
| 16 | 3 | 7.9 | 17.0 | 2.2 | 0.41 |
| 17 | 0 | 8.4 | 3.6 | 0.1 | 0.28 |
| 18 | 0 | 9.2 | 6.2 | 0.2 | 0.52 |
| 19 | 0 | 9.4 | 11.5 | 0.9 | 0.11 |
| 20 | 0 | 9.2 | 15.2 | 0.2 | 0.23 |
| 21 | 0 | 10.1 | 3.3 | 0.2 | 0.38 |
| 22 | 0 | 9.7 | 13.9 | 1.6 | 0.34 |
| 23 | 0 | 11.4 | 10.8 | 0.2 | 0.17 |
| 24 | 2 | 11.8 | 9.4 | 1.9 | 0.10 |
| 25 | 0 | 12.4 | 8.6 | 0.2 | 0.09 |
| 26 | 1 | 12.5 | 17.0 | 1.2 | 0.15 |
| 27 | 3 | 12.9 | 15.0 | 1.6 | 0.08 |
| 28 | 3 | 13.8 | 4.2 | 1.9 | 0.10 |
| 29 | 2 | 14.4 | 12.5 | 1.5 | 0.10 |

faces of the Sharkovo and Bolyarovo bodies are close to the earth's surface and reach 3- and 5-km depth, respectively. The middle, Voden body lies at a depth greater than 0.5 km and reaches 3 km in depth. At depth, the Voden and the Bolyarovo bodies come into contact (Figure 8f).

We applied the MaGSoundFDST method to the vertical component data grid from the Bolyarovo-Voden magnetic anomalous zone (Figure 8a), using a CPS set with a 3D grid spacing of $0.25 \times 0.25 \times 0.1$ km and a window of $19 \times 19$ points ($4.5 \times 4.5$ km). The lower half-space was probed down to a depth of 4 km with an upward-continuation height of 0.1 km. The inversion results are shown in Figure 8c-e. The source estimates for the Sharkovo anomaly — 2, 6, 7, 8, 10, 11, 12, and 15 — show structural indices of three and depth to the center varying from 1.4 to 1.9 km (Figure 8, Table 4). Estimates 6 and 24 are confirmed by 2.5D modeling (Figure 8f). The shallow parts of the Bolyarovo anomaly sources are detected by estimates 23 and 25, with a structural index of zero and depth of 0.2 km. Estimates 24 and 28 with a structural index of three detect the center of the sources with depth of 1.9 km. The estimates for sources 27 ($N = 3$) and 29 ($N = 2$) have depths of 1.6 and 1.5 km, respectively. The Voden anomaly estimates 18 and 21 have $N = 0$ and depth of just 0.2 km.

## CONCLUSIONS

The MaGSoundFDST procedure is based on the linearity of the FDST, and its calculation requires upward continuation of the field (a noise-suppressing procedure) or a field measured at two different observation levels. MaGSoundFDST accounts for a linear background in the anomalous field; therefore, it performs well in the presence of interfering fields. It produces a unique solution for each simple source, which is a major advantage over other window-based methods. The procedure is implemented here for regular data grids over an uneven surface, but its theoretical basis allows implementation for irregular data points obtained over uneven surfaces.

MaGSoundFDST and MaGSoundDST share several features — hence, the similar names. Both sound the subsurface for simple magnetic and gravity sources using the theory that a 3D sounding function has a minimum at the point where a source exists. In the MaGSoundFDST case, this function is an estimator of linearity of the FDST function; in MaGSoundDST, it is an estimator of linearity of the DST. The estimator of linearity of the FDST and that of the DST are calculated similarly, as the normalized residual dispersion after linear regression of the FDST and the DST, respectively. The calculation of the 3D functions, the estimators of linearity of FDST and DST, is based on the theory that the FDST and DST become linear or zero when a source exists at or near the probed point and the correct structural index for the source is used. The two procedures combine the 3D functions — the estimator of linearity of FDST and the estimator of linearity of the DST for different values of the structural index into three maps, defining the horizontal location, depth, and structural index of the sources — using the same focusing principle. Although discrete locations of the subsurface are probed, the locations of the sources are interpolated to intermediate points using a common refinement procedure.

The results from both procedures are not influenced by a linear background, an improvement over standard Euler deconvolution, which accounts only for a constant background in the measured anomalies. The difference between MaGSoundFDST and MaGSoundDST is in the way the FDST and DST are defined and hence calculated. The FDST is the difference between the measured field and an upward-continued field, so it requires an upward continuation of the field and an appropriate upward-continuation height. In contrast, the DST needs the first-order derivatives of the measured anomalies. MaGSoundFDST shows better stability than MaGSoundDST in the presence of random noise when estimating the depth and structural index of sources.

## ACKNOWLEDGMENTS

We are grateful to R. Pasteka, the associate editor, and two anonymous reviewers for their constructive suggestions and encouragement to improve the manuscript. This work was funded by Natural Research Council (U.K.) grant NER/0/S/2003/00674.

## REFERENCES


Blakely, R. J., 1995, Potential theory in gravity and magnetic applications: Cambridge University Press.

Boukerbout, H., and D. Gibert, 2006, Identification of sources of potential fields with the continuous wavelet transform: Two-dimensional ridgelet analysis: Journal of Geophysical Research, **111**, B07104.

Courant, R., and F. John, 1965, Introduction to calculus and analysis: Wiley Interscience.

Fedi, M., 2007, DEXP: A fast method to determine the depth and the structural index of potential field sources: Geophysics, **72**, no. 1, I1–I11.

Fedi, M., G. Florio, and T. A. M. Quarta, 2009, Multiridge analysis of potential fields: Geometric method and reduced Euler deconvolution: Geophysics, **74**, no. 4, L53–L65.

Fedi, M., and A. Rapolla, 1999, 3-D inversion of gravity and magnetic data with depth resolution: Geophysics, **64**, 452–461.

FitzGerald, D., A. Reid, and P. McInerny, 2004, New discrimination techniques for Euler deconvolution: Computers & Geosciences, **30**, 461–469.

Gerovska, D., and M. J. Araúzo-Bravo, 2003, Automatic interpretation of magnetic data based on Euler deconvolution with unprescribed structural index: Computers & Geosciences, **29**, 949–960.

——–, 2006, Calculation of magnitude magnetic transforms with high centricity and low dependence on the magnetization vector direction: Geophysics, **71**, no. 4, I21–I30.

Gerovska, D., M. J. Araúzo-Bravo, P. Stavrev, and K. Whaler, 2010, MaGSoundDST — Three-dimensional automatic inversion of magnetic and gravity data based on the finite difference similarity transform: Geophysics, **75**, no. 1, L25–L38.

Gerovska, D., P. Stavrev, and M. J. Araúzo-Bravo, 2005, Finite-difference Euler deconvolution algorithm applied to the interpretation of magnetic data from northern Bulgaria: Pure and Applied Geophysics, **162**, 591–608.

Hsu, S. K., 2002, Imaging magnetic sources using Euler's equation: Geophysical Prospecting, **50**, 15–25.

Keating, P., and M. Pilkington, 2004, Euler deconvolution of the analytic signal and its application to magnetic interpretation: Geophysical Prospecting, **52**, 165–182.

Reid, A. B., J. M. Allsop, H. Granser, A. J. Millet, and I. W. Somerton, 1990, Magnetic interpretation in three dimensions using Euler deconvolution: Geophysics, **55**, 80–91.

Reid, A. B., D. FitzGerald, and G. Flanagan, 2005, Hybrid Euler magnetic basement estimation: Bishop 3D tests: 75th Annual International Meeting, SEG, Expanded Abstracts, 671–673.

Sailhac, P., D. Gibert, and H. Boukerbout, 2009, The theory of the continuous wavelet transform in the interpretation of potential fields: A review: Geophysical Prospecting, **57**, 517–525.

Salem, A., S. Williams, D. Fairhead, R. Smith, and D. Ravat, 2008, Interpretation of magnetic data using tilt-angle derivatives: Geophysics, **73**, no. 1, L1–L10.

Stavrev, P. Y., 1997, Euler deconvolution using differential similarity transformations of gravity or magnetic anomalies: Geophysical Prospecting, **45**, 207–246.

Stavrev, P., and D. Gerovska, 2000, Magnetic field transforms with low sensitivity to the direction of source magnetization and high centricity: Geophysical Prospecting, **48**, 317–340.

Stavrev, P., D. Gerovska, and M. J. Araúzo-Bravo, 2006, Automatic inversion of magnetic anomalies from two height levels using finite-difference similarity transforms: Geophysics, **71**, no. 6, L75–L86.

——–, 2009, Depth and shape estimates from simultaneous inversion of magnetic fields and their gradient components using differential similarity transforms: Geophysical Prospecting, **57**, 707–717.

Stavrev, P., and R. Raditchev, 1998, Depth characteristics of plutonic bodies in the Strandza intrusive zone according to magnetic data: Bulgarian Geophysical Journal, **24**, 100–110.

Thompson, D. T., 1982, EULDPH: A new technique for making computer-assisted depth estimates from magnetic data: Geophysics, **47**, 31–37.

Williams, S. E., J. D. Fairhead, and G. Flanagan, 2002, Realistic models of basement topography for depth to magnetic basement testing: 72nd Annual International Meeting, SEG, Expanded Abstracts, 814–817.

——–, 2005, Comparison of grid Euler deconvolution with and without 2D constraints using a realistic 3D magnetic basement model: Geophysics, **70**, no. 3, L13–L21.